Journal of Materials Chemistry A

Improving LiNiO2 cathode performance through particle design and optimization

Journal:	*Journal of Materials Chemistry A*
Manuscript ID	TA-ART-03-2022-002492.R1
Article Type:	Paper
Date Submitted by the Author:	04-May-2022
Complete List of Authors:	Kim, Minkyung; Lawrence Berkeley National Laboratory, ESDR Zou, Lianfeng; Pacific Northwest National Laboratory Son, Seoung-Bum ; Argonne National Laboratory Bloom, Ira; Argonne National Laboratory Wang, Chongmin; Pacific Northwest National Laboratory, Environmental Molecular Sciences Laboratory Chen, Guoying; Lawrence Berkeley National Laboratory, ESDR

Improving $LiNiO_2$ cathode performance through particle design and optimization

Minkyung Kim,[a,b] Lianfeng Zou,[c] Seoung-Bum Son,[d] Ira D. Bloom,[d] Chongmin Wang [c] and Guoying Chen [a,]*

[a] *Energy Storage and Distributed Resources Division, Lawrence Berkeley National Laboratory, Berkeley, California 94720, USA*

[b] *Department of Electronic material Engineering, Kwangwoon University, 20, Gwangun-ro, Nowon-gu, Seoul 01897, Republic of Korea*

[c] *Environmental Molecular Sciences Laboratory, Pacific Northwest National Laboratory, Richland, WA 99354, USA*

[d] *Chemical Sciences and Engineering Division, Argonne National Laboratory. Argonne, Illinois 60439, USA*

** Corresponding author's email:* gchen@lbl.gov

Abstract

To enable further development of Ni-rich $LiNi_xMn_yCo_{1-x-y}O_2$ (NMC, $x \geq 0.9$) cathodes for commercial applications, fundamental understanding of the synthesis-property-performance relationships in $LiNiO_2$ (LNO) parent phase is essential. In the present study, we report synthesis approaches to produce well-formed, similar-sized single-crystal $LiNiO_2$ (SC-LNO) with different shapes and dominating surface facets, and reveal the dependence of cathode rate performance and cycling stability on particle morphology and surface. While octahedron-shaped SC-LNO with the (012) surface shows better rate capability and improved ability in utilizing the kinetically slow anodic process in the 3.5 V region, cubic-shaped SC-LNO with the (104) surface delivers superior cycling stability, especially upon cycling at a high upper cutoff voltage of 4.6 V. Improvement in cycling stability is correlated to reduced surface reconstruction and preferential LiF formation through the interaction with the electrolyte on the (104) surface. Our study not only demonstrates the importance of particle morphology and surface design, it also provides key insights on desirable materials properties for developing future LNO-based cathode materials with better performance.

1. Introduction

For large-scale applications, such as electrical vehicles, lithium-ion batteries (LIBs) with higher energy density, better stability and lower cost are needed.[1-3] Ni-rich layered transition-metal oxide cathodes such as $LiNi_xCo_yAl_{1-x-y}O_2$ and $LiNi_xMn_yCo_{1-x-y}O_2$ (NMC, $x > 0.9$) are currently considered most promising in meeting these requirements.[4-5] This is largely due to the high charge storage capacity and energy density provided by the high nickel content (x). However, as x approaches 1.0 in these layered systems, the material properties increasingly resemble that of the parent phase, $LiNiO_2$ (LNO). In order to further develop Ni-rich oxide cathode materials, a better understanding of structure-properties-performance corrections in LNO is essential.[6]

The challenges associated with LNO-based cathode materials often include the following: 1) morphological damage, such as particle cracking due to phase transformation and volume changes;[7-9] 2) structural transformation from layered to spinel-like and/or rocksalt-type phases, especially on the surface;[10-12] 3) parasitic reactions between cathode and the electrolyte;[13-16] and 4) thermal instabilities associated with the high reactivity of Ni.[17] To address these issues, previous research mostly focused on bulk material modifications. For example, bulk doping with various dopants, such as W, Mg, B etc., was heavily investigated as a way to enhance the stability of Ni-rich NMC and LNO-type cathodes.[18-27] Doping was found to reduce anisotropic lattice parameter variations during charge and discharge, thereby reducing capacity fade due to particle cracking and morphological damage.

In recent years, research effort on layered oxides has revealed the important role of particle surface on cathode reactivity and cycling stability. For example, density functional theory (DFT) calculations carried out on $LiCoO_2$ and $LiNi_{0.33}Mn_{0.33}Co_{0.33}O_2$ determined that their equilibrium particle shapes are consisting of (104), (001) and (012) facets, and that the (104)-family facets are

more stable than (012) facets during electrochemical cycling.[28] Experimentally, oxygen release and thermal decomposition of $LiCoO_2$ were found to be facet-dependent, and structural reconstruction from the layered to spinel-like and rocksalt-type phases occurred preferably on (012)- and (104)-family facets, as opposed to the (001)-family facets.[29] Recently, intra-granular cracking resulting from high-voltage cycling of the layered oxides was found to progress from the grain interior along the (003) planes, which led to bulk structural degradation and reduced long-term stability.[30-31]

Similar surface-related studies on LNO, however, are relatively unexplored. A large factor is the nature of particles obtained through the conventional co-precipitation method, which often produces porous aggregates of secondary particles consisting of various sized primary particles. As material performance is controlled by the physical properties of primary particles as well as the properties of the secondary particles, such as particle size distribution, porosity, grain boundaries, etc., it is simply impossible to isolate the impact of a particular material's property, such as surface orientation, in these studies.

Herein, we developed approaches to synthesize discrete, LNO single crystals with different morphologies and surface facets. We show that Cubic-SC-LNO with dominating (104) surface; Oct-SC-LNO with dominating (012) surface; and T-poly-SC-LNO with mixed surface facets can be prepared by varying the molten flux used during the reaction. We further use this series of samples to correlate the impact of particle morphology and surface to cathode rate capacity and cycling stability. Our findings suggest that key LNO performance indicators, including Li transport properties, cycling-induced surface reconstruction and cathode-electrolyte interphase (CEI) composition, strongly depend on particle surface facet, a result of varying Li diffusion channels and Fermi levels due to the specific atomic arrangements of each facet.

2. Results and Discussion

2.1. Synthesis and characterization of SC-LNO

Molten-salt synthesis was used to prepare LNO single crystals with controlled particle size and morphology. The procedure was similar to what was described in detail in our previous publications.[32-33] Several factors, including the chemical nature of the precursors and the flux, the mole ratio between the transition-metal (TM) and the flux (defined as the R ratio), reaction atmosphere, soaking temperature/time and the heating and cooling rates, can influence the uniformity and physical attributes of the synthesized crystals.[32] For LNO, $Ni(NO_3)_2 \cdot 6H_2O$ and LiOH were used as reaction precursors. By using a mixture of Li_2SO_4-LiOH (1:4 mol ratio, m. p. = 350 °C) as a flux and an R ratio of 2, LNO single crystals with the cubic particle shape (referred to as Cubic-SC-LNO hereafter) were obtained. At a higher R ratio of 4, we prepared octahedron-shaped SC-LNO (referred to as Oct-SC-LNO hereafter) from a KCl-LiCl (2:3 mol ratio, m. p. = 405 °C) flux. Truncated-polyhedron-shaped SC-LNO single crystals (referred to as T-poly-SC-LNO hereafter) were obtained from a CsCl flux (m. p. = 645 °C) with an R ratio of 2. All syntheses were carried out at the same calcination temperature of 750 °C for 10h followed by an annealing step at 700 °C for 2h. The samples had the same average particle size of ~ 1 μm as shown in the SEM images (Figure 1a-c). Phase-pure, hexagonal, α-$NaFeO_2$-type structure with the $R\bar{3}m$ space group was confirmed by X-ray diffraction (XRD) analysis (Figure 1d-f). The clearly resolved peak splitting of the (108)/(110) doublets shown in the insets of Figure 1d-f confirms well-layered crystal structure in all samples. Lattice dimensions and the degree of Li/Ni cation mixing were obtained from Rietveld refinement of the XRD patterns and the results are shown in Table 1. The differences in the lattice parameters are insignificant; however, a slightly higher degree of cation

mixing was observed on Oct-SC-LNO. The chemical composition was further analyzed by inductively coupled plasma (ICP) measurements, which confirm the stoichiometric $LiNiO_2$ chemistry in all samples.

Previous density functional theory (DFT) calculations reported that in layered-structured $LiTMO_2$ such as $LiCoO_2$ and NMCs, the thermodynamically-equilibrated particle shapes are typically enclosed by three dominant families of surface facets, namely (104), (001) and (012). [28, 34-35] While the (001) plane is parallel to the Li and TM slabs in the crystal structure and is known to be Li-ion impermeable, both (012) and (104) facets are terminated with alternating TM-O-Li slabs and consequently Li-permeable. Among them, the surface energy of the (012) and (104) facets are the highest and lowest, respectively. In order to determine surface facets on each SC-LNO samples, focused ion beam (FIB) was used to section the single crystals, which were then examined for exposed planes on the edges by using high-resolution transmission electron microscopy (HRTEM). Figure 1g-i show the surface facets that are present in Cubic-SC-LNO, Oct-SC-LNO and T-poly-SC-LNO, respectively. The Cubic-SC-LNO particles are enclosed predominately by (104)-family planes along with a small fraction of (012) planes. For Oct-SC-LNO particles, (012)-family planes dominate the surface while a small amount of (001) also present. The T-poly-SC-LNO particles are enclosed by a mixture of planes including (001), (012), (104), (010) and $(0\bar{1}1)$. Based on these analysis results, 3D crystal shapes were constructed by using visualization for electronic and structure analysis (VESTA) software program and are shown in Figure 1g-i insets. It is clear that while the surfaces of Cubic-SC-LNO and Oct-SC-LNO can be assigned as (104)-family and (012)-family, respectively, T-poly-SC-LNO particles are enclosed with a mixture of facets without a clear dominating surface orientation.

2.2. Electrochemical performance of SC-LNO

Electrochemical properties of as-synthesized $LiNiO_2$ single crystals were evaluated at room temperature in a half-cell coin-cell configuration. Composite cathodes were prepared by mixing SC-LNO, poly(vinylidene fluoride) (PVDF) binder and acetylene black in a weight ratio of 80:15:5. Figure 2 compares the voltage profiles (Figure 2a-c) and the corresponding differential capacity *vs.* voltage (dQ/dV) plots (Figure 2d-f) at various charge and discharge rates. At 0.01C (1C = 180 mAh/g), all three samples displayed similar voltage profiles with charge/discharge capacities of about 260/230 mAh/g, corresponding to an initial coulombic efficiency (CE) of ~ 90%. A voltage plateau near 3.5 V is clearly shown on all discharge profiles, indicating capacity contribution from the anodic redox process occurring in that window. Upon increasing the rate to 0.02C, the discharge capacities decreased to about 218 mAh/g. Interestingly, while the 3.5 V plateau disappeared in the cells with either a Cubic-SC-LNO (Figure 2a and d) or T-poly-SC-LNO cathode (Figure 2c and f), it largely remained in the cell with the Oct-SC-LNO cathode (Figure 2b and e). Further increasing the rate to 0.1C reduces the discharge capacities to about 210 mAh/g, along with the disappearance of the 3.5 V plateau in all samples. Although the redox reactions at 3.5 V plateau is currently not well understood, earlier studies suggested a kinetically sluggish process that can enhance LNO cathode capacity when activated.[36-37] For the first time, our results reveal that particle morphology plays an important role in extracting the capacity from the 3.5 V region. Oct-SC-LNO with the (012) surface is capable of better activating and utilizing the redox process in that region. Further studies are necessary in order to gain fundamental understanding on the correlations as well as how to best utilize them in martials development.

Kinetic properties of SC-LNO samples were further evaluated by carrying out the rate capability tests, where the same charge rate of 0.1C was used while the discharge rate varied from

0.1C to 10C (Figure 3 and Figure S1). For Cubic-SC-LNO, the discharge capacities were 205, 196, 192, 177, 165, 155, 144 and 130 mAh/g at 0.1C, 0.3C, 0.5C, 1C, 2C, 3C, 5C and 10C, respectively (Figure 3a). Nearly 65% of capacity remained when increasing the rate from 0.1C to 10C. The discharge capacities of Oct-SC-LNO were 212, 206, 199, 188, 180, 168, 159 and 144 mAh/g at 0.1C, 0.3C, 0.5C, 1C, 2C, 3C, 5C and 10C, respectively (Figure 3b). When increasing the rate from 0.1C to 10C, a slightly higher capacity retention of ~ 68 % was achieved. The rate capability of T-poly-SC-LNO, on the other hand, was significantly poorer, with only about 27% capacity retention obtained at 10C (Figure 3c). The slightly improved the kinetic properties of Oct-SC-LNO, as shown in Figure 3d and Figure S1, is likely a result of atomic arrangement of the (012) plane on the surface. Although both (012) and (104) planes have Li diffusion pathways, the calculated areas per Li diffusion channel (or per Li site) are 15.91 $Å^2$ and 11.7 $Å^2$ for (104) and (012) planes, respectively. This suggests that for a given surface area, more Li sites are available on (012) than (104), rendering more favorable kinetics in the former. In the case of T-poly-SC-LNO, the poorer kinetics can be attributed to the high fraction of (001) plane on the surface which is Li impermeable.[34]

We wish to emphasize that the rate capability of both Oct-SC-LNO and Cubic-SC-LNO are comparable to that of the state-of-the-art $LiNiO_2$ prepared by the co-precipitation method, even though our samples consist of micron-sized single crystals whereas the traditional LNO particles are often polycrystalline consisting of nanosized primary particles.[38-39] While particle size is well known for its role in kinetics and size reduction is often used as a strategy in improving rate capability,[40-42] here we clearly demonstrate the importance of particle morphology and surface in controlling kinetic properties. In commercial applications, the ability to achieve high rate capacity without resorting to small-sized cathode active particles is essential as it eliminate the challenges

associated with high surface area, such as enhanced side reactions with the electrolyte as well as the need of using more inactive components (carbon and binder) during electrode fabrication. We believe particle engineering offers an viable route to cathode materials with better rate capabilities.

Long-term cycling stability comparison of the SC-LNO cathodes, carried out at 0.1C charge/discharge for the first two cycles followed by 0.3C in the voltage window of 2.7-4.3 V and 2.7-4.6 V are shown in Figure 4. Upon cycling to 4.3 V (Figure 4a-c), both Cubic-SC-LNO and Oct-SC-LNO had a similar initial discharge capacity of ~ 205 mAh/g at 0.1C and 190 mAh/g at 0.3C. T-poly-SC-LNO had a slightly higher initial capacity of ~ 215 mAh/g at 0.1C which decreased to 180 mAh/g at 0.3C rate. After 100 cycles, the discharge capacities were reduced to ~ 144, 135 and 120 mAh/g for Oct-SC-LNO, Cubic-SC-LNO and T-poly-SC-LNO respectively, corresponding to capacity retention of about 76%, 72% and 67%. (Figure 4g). As expected, increasing the upper cutoff voltage (UCV) to 4.6 V increases the initial capacity but reduces cycling stability. For all three samples, about 215 and 200 mAh/g were obtained at 0.1C and 0.3C, respectively (Figure 4d-f). After 100 cycles, the discharge capacity was reduced to ~ 130, 102 and 85 mAh/g for Cubic-SC-LNO, Oct-SC-LNO and T-poly-SC-LNO, respectively, corresponding to a capacity retention of about 65%, 51% and 42% (Figure 4h). The degree of capacity retention reduction is therefore 11% for Cubic-SC-LNO, 21% for Oct-SC-LNO and 25% for T-poly-SC-LNO, when increasing the UCV from 4.3 V to 4.6 V (Figure 4i). While the trends in coulombic efficiency are largely similar in all cycling stability tests, the excellent stability of Cubic-SC-LNO with the (104) surface was demonstrated not only by the superior cycling stability at both 4.3 V and 4.6 V UCV, but also by the enhanced stability under high voltage operation, compared to that of the other SC-LNO samples in the series.

2.3. Understanding the origin of performance differences

Post-modem analyses were carried out in order to understand the different cycling behavior observed on the SC-LNO samples. Scanning transmission electron microscopy-high angle annular dark field (STEM-HAADF) imaging was used to examine the structural changes at the atomic level. It is well known that these images provide brightness contrast that is proportional to the atomic number of the atoms present, enabling the differentiation of heavy atoms (such as transition metals) from light atoms (such as Li). The technique is widely used to monitor surface reconstruction (SR) in layered oxide cathodes where the appearance of brightness in the Li layers increases upon the structural transformation from the layered to spinel-like or rocksalt-type phases. In general, SR is induced by lattice oxygen loss and the subsequent site mixing between Li and Ni cations.[11, 33, 43]

Figure 5 compares the STEM-HAADF images collected on the various facets of the pristine and discharged SC-LNO particles after 100 cycles. For the pristine series (Figure 5a-e), while bright spots are not observed in the lithium layers in the bulk, their presence is clearly seen on the top few atomic layers of all surface facets examined, indicating a thin native SR on as-synthesized SC-LNO particle surface. This is consistent with what was reported in the literature.[44-45]

After cycling, a varying degree of further surface reconstruction was observed on the facets, with the SR thickness increased to 2.5, 2.6, 2.1, 5.1 and 7.0 nm for (104), (012), (001), (0 $\bar{1}$1) and (010) facets, respectively (Figure 5f-j). (104), (012) and (001) surfaces experienced a similar level of further reconstruction during cycling, whereas (010) and (0$\bar{1}$1) surface planes had

a significantly higher level of changes. These results are consistent with the observed cycling behavior, where Cubic-SC-LNO with the dominating (104) surface and T-poly-SC-LNO with the mixed surface facets delivered the best and worst cycle stabilities in the series, respectively. The origin of surface reconstruction and how different facets affect the reconstruction process were reported in our previous publications.[28, 33, 43] Density Functional Theory (DFT) calculations revealed facet-dependent segregation in NMC cathodes. Particularly, Co tends to segregate to the (104) surface within the transition-metal layer while Ni ions tend to segregate to the (012) surface in the Li layer, promoting different surface reconstruction behavior. Our experimental results further support these calculations.

Further analysis on surface changes was carried out by using X-ray photoelectron spectroscopy (XPS). As Li ion is extracted during charge, the Fermi level of traditioal LNO surface often moves closer to that of electrolyte, leading to side reactions with the electrolyte and deposition of various organic and inorganic decomposition products.[46-48] Figure 6 shows C 1*s*, O 1*s* and F 1*s* spectra collected on the discharged SC-LNO cathodes after 100 cycles. All samples showed similar C 1*s* spectra with the presence of peaks attributed to C-C, C-O, C=O, O-C=O and CF_2 (Figure 6a-c). For O 1*s*, peaks at 529.5, 532.4 and 534.1 eV are attributed to Ni-O (lattice oxygen), C=O and C-O bonding, respectively (Figure 6d-f).[48] In Ni-rich layered oxides, the intensity of O 1*s* peak from lattice oxygen often decreases with cycling due to the shielding effect from the electrolyte decomposition products deposited on the surface. Compared to that in Oct-SC-LNO and T-poly-SC-LNO (Figure 6e and f), the O 1*s* peak from Ni-O is noticeably stronger in the cycled Cubic-SC-LNO sample (Figure 6d), suggesting reduced presence of side reaction products on the surface. Significant differences were observed on the F 1*s* spectra where peaks at 685.2, 686.2, and 688.0 eV can be attributed to LiF, $Li_xPO_yF_z$ and CF_2, respectively (Figure 6g-

i).[49] Much higher LiF peak intensity was found on the cycled Cubic-SC-LNO cathode (Figure 6i), suggesting preferential formtion of LiF product on the (104) surface. The presence of LiF-rich cathode-electrolyte interphase has previously been shown to provide surface protection against HF and other free radical compounds in the electrolyte, leading to enhanced cathode stability.[48] Our results further confirm the positive effect of surface LiF presence on cycling stability.

To the best of our knowledge, this is the first report on the dependence of CEI chemical compositions on particle morphology and surface of the same bulk material. The origin may be traced back to the different atomic arrangements of the surface crystalline planes, which results in different Fermi levels.[46, 50] Among the surface planes examined in this study, (012), (003) and (101) belong to the family of polar planes while (104) belongs to the nonpolar family.[46] Calculations have shown that the Fermi level in polar planes decreases as lithium ions are extracted while that of the nonpolar facet often remains stable regardless of the lithium content.[46] This leads to a significantly more reactive surface in the former whereas the latter more or less remains the same at the charged state. In the presence of a $LiPF_6$-based liquid electrolyte, the polar (012) surface on Oct-SC-LNO may continue to decompose the electrolyte at high voltages and form $Li_xPO_yF_z$ -rich CEI. On the other hand, Cubic-SC-LNO with the (104) surface forms more stable LiF-rich CEI layer which ultimately leads to better cycling stability of the cathode. To this end, maximizing surface presence of nonpolar facet such as (104) while minimizing polar facets such as (003), (012) and (101) is likely an effective strategy in improving LNO cathode stability. Clearly, the hypothesis requires further studies combining both theory and experimental investigations. Related work is currently underway and we will report the results in a future publication.

3. Experimental

3.1. Synthesis

Stoichiometric amounts of LiOH (> 98%, *Sigma Aldrich*) and $Ni(NO_3)_2 \cdot 6H_2O$ (98%, *Alfa Aesar*) were used as lithium and nickel precursors, respectively. A selected molten-salt, Li_2SO_4-LiOH, LiCl-KCl or CsCl (*Sigma Aldrich*), was mixed thoroughly with the lithium and nickel precursors using mortar and pestle, in a mole ratio shown in Table S1. The mixed powders were preheated at 450°C for 2 h at a 4.5 °C/min ramping rate and then annealed at 750°C for 10 h under an oxygen gas flow, before cooling down at a rate of 5°C/min. The obtained samples were washed by deionized water to dissolve residue salts and then centrifuged at 9000 rpm to remove all soluble salts thoroughly. The final product was obtained by further annealing at 700°C for 2 h under an oxygen flow.

3.2. Characterization

X-ray diffraction was carried out using a Bruker D2 powder X-ray diffractometer (Cu Kα, 40 kV and 30 mA) with a step size of 0.02° and a data collection time of 10 s per step. The collected scattering angle (2Θ) range was 10-85°. Morphologies were evaluated by scanning electron microscope (JEOL JSM-7500F field emission) at a 10 kV accelerating voltage. To eliminate the charging effect, powder samples were sputtered with a thin Au layer before conducting SEM. Chemical compositions were confirmed using inductively coupled plasma-optical emission spectrometry (ICP-OES, Perkin-Elmer Optima 5300 DV). For scanning transmission electron microscopy analysis, an electron transparent lamellar was extracted from the cathode particle using

focus ion beam lifting out technique (Helios system with Ga ion, Thermofisher Scientific). The thin section was thinned step by step at the voltage of 30 kV and the final polishing was performed at 2 kV. The High-angle annular darkfield imaging (HAADF-STEM) imaging were performed on the probe aberration corrected JEOL JEM-ARM200CF operated at a voltage of 200 kV. STEM high-angle annular dark-field (HAADF) imaging was performed on an aberration-corrected JEOL JEM-ARM200CF microscopy with the operation voltage of 200 kV. The convergence semi-angle is 20.6 mrad, and the collection semi-angles span from 90 to 370 mrad.

XPS measurements were carried out using a PHI 5000 VersaProbe II System (Physical Electronics). Samples were transferred without air exposure in an argon-atmosphere glovebox connected to the XPS system. The spectra were obtained using Al K*a* radiation (hν = 1486.6 eV, 100 μm, 25 W), Ar^+ and electron beam sample neutralization in a fixed analyzer transmission mode. The XPS binding energies were calibrated to the carbon black component in the C 1*s* spectra at 284.8 eV. Peak fitting was performed using Shirley background correction and the Gaussian–Lorentzian curve synthesis available in the MultiPack® software.

3.3. Electrochemical evaluation

The as-prepared $LiNiO_2$ single crystals, poly(vinylidene fluoride) binder (Kynar 2801) and acetylene black conductive additive (Denka) were mixed together in a N-methylpyrrolidone (NMP, Sigma Aldrich) solvent in a weight ratio of 80:15:5. The slurry was coated onto a carbon-coated aluminum foil current collector and dried at 120 °C in a vacuum oven overnight. Electrodes were cut out with an area of 1.6 cm^2 and an average active mass loading of ~ 2 mg/cm^2. Half cells were assembled in 2032-type coin cells in argon-filled glovebox using Li foil (Alfa-Aesar) as both

counter and reference electrodes. Celgard 2400 membrane was used as a separator, and Gen 2 electrolyte (1.2M $LiPF_6$ in EC/EMC 3:7) was added to the coin cells before sealing. Electrochemical performance was evaluated at ambient temperature on a VMP3 multichannel potentiostat/galvanostat controlled by EC-Lab software (Bio-Logic Science Instruments).

4. Conclusions

Three $LiNiO_2$ single-crystal samples were synthesized in the same particle size but with different morphologies and surface facets. The dominating surface facets were determined to be (104)-family and (012)-family for Cubic-SC-LNO and Oct-SC-LNO, respectively, whereas T-poly-SC-LNO particles were enclosed by a mixture of surface facets including (001), (012), (104), (010) and $(0\bar{1}1)$. These high-quality samples allowed us to clearly illustrate the critical role of particle morphology and surface plays in cathode kinetics and cycling stability. While better kinetics were achieved on (012)-surfaced Oct-SC-LNO cathode, (104)-surfaced Cubic-SC-LNO showed superior stability with improved capacity retention when cycled either with a 4.3 V or 4.6 V UCV. HAADF-STEM analysis showed a similar level of cycling-induced surface reconstruction on (003), (104) and (012) facets whereas the (010) and $(0\bar{1}1)$ facets on the T-poly-SC-LNO particles had a significantly thicker SRL, consequently lower capacity retention of T-poly-SC-LNO cathode. In addition, preferential LiF formation was found on the (104) surface which contributes to the improved cycling stability observed on Cubic-SC-LNO. Our study demonstrates the importance of morphology/surface tailoring and provides critical insights for future development of LNO-based cathodes with improved performance.

Conflicts of Interest

There are no conflicts of interest to declare

Acknowledgements

The authors thank Drs. Yanying Lu and Faxing Wang at LBNL for proof reading the manuscript, and thank Drs. Jason Croy, Hakim Iddir, Eungje Lee and Jihyeon Gim at ANL for fruitful discussions. The TEM work was conducted at the William R. Wiley Environmental Molecular Sciences Laboratory (EMSL), a national scientific user facility sponsored by DOE's Office of Biological and Environmental Research and located at PNNL. PNNL is operated by Battelle for the Department of Energy under Contract DE-AC05-76RLO1830. Argonne National Laboratory is operated for the DOE Office of Science by UChicago Argonne, LLC, under contract number DE-AC02-06CH11357. This work was supported by the Assistant Secretary for Energy Efficiency and Renewable Energy, Office of Vehicle Technologies of the U.S. Department of Energy under Contract No. DE-AC02-05CH11231.

References

1. Xia, Y.; Zheng, J. M.; Wang, C. M.; Gu, M., Designing principle for Ni-rich cathode materials with high energy density for practical applications. *Nano Energy* **2018,** *49*, 434-452.

2. Tian, Y.; Zeng, G.; Rutt, A.; Shi, T.; Kim, H.; Wang, J.; Koettgen, J.; Sun, Y.; Ouyang, B.; Chen, T.; Lun, Z.; Rong, Z.; Persson, K.; Ceder, G., Promises and Challenges of Next-Generation "Beyond Li-ion" Batteries for Electric Vehicles and Grid Decarbonization. *Chem Rev* **2021,** *121* (3), 1623-1669.

3. Manthiram, A., A reflection on lithium-ion battery cathode chemistry. *Nat Commun* **2020,** *11* (1).

4. Li, W.; Lee, S.; Manthiram, A., High-Nickel NMA: A Cobalt-Free Alternative to NMC and NCA Cathodes for Lithium-Ion Batteries. *Advanced Materials* **2020,** *32* (33), 2002718.

5. Choi, J. U.; Voronina, N.; Sun, Y.-K.; Myung, S.-T., Recent Progress and Perspective of Advanced High-Energy Co-Less Ni-Rich Cathodes for Li-Ion Batteries: Yesterday, Today, and Tomorrow. *Advanced Energy Materials* **2020,** *10* (42), 2002027.

6. Xu, C.; Marker, K.; Lee, J.; Mahadevegowda, A.; Reeves, P. J.; Day, S. J.; Groh, M. F.; Emge, S. P.; Ducati, C.; Mehdi, B. L.; Tang, C. C.; Grey, C. P., Bulk fatigue induced by surface reconstruction in layered Ni-rich cathodes for Li-ion batteries. *Nat Mater* **2021,** *20* (1), 84-92.

7. Ryu, H.-H.; Park, K.-J.; Yoon, C. S.; Sun, Y.-K., Capacity Fading of Ni-Rich Li[NixCoyMn1−x−y]O2 (0.6 ≤ x ≤ 0.95) Cathodes for High-Energy-Density Lithium-Ion Batteries: Bulk or Surface Degradation? *Chem Mater* **2018,** *30* (3), 1155-1163.

8. Yin, S.; Deng, W.; Chen, J.; Gao, X.; Zou, G.; Hou, H.; Ji, X., Fundamental and solutions of microcrack in Ni-rich layered oxide cathode materials of lithium-ion batteries. *Nano Energy* **2021,** *83*, 105854.

9. Xu, C.; Reeves, P. J.; Jacquet, Q.; Grey, C. P., Phase Behavior during Electrochemical Cycling of Ni-Rich Cathode Materials for Li-Ion Batteries. *Advanced Energy Materials* **2021,** *11* (7), 2003404.

10. Tornheim, A.; Sharifi-Asl, S.; Garcia, J. C.; Bareno, J.; Iddir, H.; Shahbazian-Yassar, R.; Zhang, Z. C., Effect of electrolyte composition on rock salt surface degradation in NMC cathodes during high-voltage potentiostatic holds. *Nano Energy* **2019,** *55*, 216-225.

11. Lin, F.; Markus, I. M.; Nordlund, D.; Weng, T.-C.; Asta, M. D.; Xin, H. L.; Doeff, M. M., Surface reconstruction and chemical evolution of stoichiometric layered cathode materials for lithium-ion batteries. *Nat Commun* **2014,** *5* (1), 3529.

12. Liang, L.; Zhang, W.; Zhao, F.; Denis, D. K.; Zaman, F. u.; Hou, L.; Yuan, C., Surface/Interface Structure Degradation of Ni-Rich Layered Oxide Cathodes toward Lithium-Ion Batteries: Fundamental Mechanisms and Remedying Strategies. *Advanced Materials Interfaces* **2020,** *7* (3), 1901749.

13. Takahashi, I.; Kiuchi, H.; Ohma, A.; Fukunaga, T.; Matsubara, E., Cathode Electrolyte Interphase Formation and Electrolyte Oxidation Mechanism for Ni-Rich Cathode Materials. *J Phys Chem C* **2020,** *124* (17), 9243-9248.

14. Xue, W.; Huang, M.; Li, Y.; Zhu, Y. G.; Gao, R.; Xiao, X.; Zhang, W.; Li, S.; Xu, G.; Yu, Y.; Li, P.; Lopez, J.; Yu, D.; Dong, Y.; Fan, W.; Shi, Z.; Xiong, R.; Sun, C.-J.; Hwang, I.; Lee, W.-K.; Shao-Horn, Y.; Johnson, J. A.; Li, J., Ultra-high-voltage Ni-rich layered cathodes in practical Li metal batteries enabled by a sulfonamide-based electrolyte. *Nature Energy* **2021,** *6* (5), 495-505.

15. Yan, P.; Zheng, J.; Liu, J.; Wang, B.; Cheng, X.; Zhang, Y.; Sun, X.; Wang, C.; Zhang, J.-G., Tailoring grain boundary structures and chemistry of Ni-rich layered cathodes for enhanced cycle stability of lithium-ion batteries. *Nature Energy* **2018,** *3* (7), 600-605.

16. Zhang, X. H.; Jia, H.; Zou, L. F.; Xu, Y. B.; Mu, L. Q.; Yang, Z. J.; Engelhard, M. H.; Kim, J. M.; Hu, J. T.; Matthews, B. E.; Niu, C. J.; Wang, C. M.; Xin, H. L.; Lin, F.; Xu, W., Electrolyte Regulating toward Stabilization of Cobalt-Free Ultrahigh-Nickel Layered Oxide Cathode in Lithium-Ion Batteries. *Acs Energy Letters* **2021,** *6* (4), 1324-1332.

17. Bak, S. M.; Hu, E. Y.; Zhou, Y. N.; Yu, X. Q.; Senanayake, S. D.; Cho, S. J.; Kim, K. B.; Chung, K. Y.; Yang, X. Q.; Nam, K. W., Structural Changes and Thermal Stability of Charged LiNixMnyCozO2 Cathode Materials Studied by Combined In Situ Time-Resolved XRD and Mass Spectroscopy. *Acs Applied Materials & Interfaces* **2014,** *6* (24), 22594-22601.

18. Xie, Q.; Li, W.; Manthiram, A., A Mg-Doped High-Nickel Layered Oxide Cathode Enabling Safer, High-Energy-Density Li-Ion Batteries. *Chem Mater* **2019,** *31* (3), 938-946.

19. Kim, U.-H.; Park, G.-T.; Son, B.-K.; Nam, G. W.; Liu, J.; Kuo, L.-Y.; Kaghazchi, P.; Yoon, C. S.; Sun, Y.-K., Heuristic solution for achieving long-term cycle stability for Ni-rich layered cathodes at full depth of discharge. *Nat Energy* **2020,** *5* (11), 860-869.

20. Kim, U.-H.; Park, N.-Y.; Park, G.-T.; Kim, H.; Yoon, C. S.; Sun, Y.-K., High-Energy W-Doped Li[Ni0.95Co0.04Al0.01]O2 Cathodes for Next-Generation Electric Vehicles. *Energy Storage Materials* **2020,** *33*, 399-407.

21. Ryu, H. H.; Park, G. T.; Yoon, C. S.; Sun, Y. K., Suppressing detrimental phase transitions via tungsten doping of LiNiO2 cathode for next-generation lithium-ion batteries. *Journal of Materials Chemistry A* **2019,** *7* (31), 18580-18588.

22. Yoon, C. S.; Kim, U.-H.; Park, G.-T.; Kim, S. J.; Kim, K.-H.; Kim, J.; Sun, Y.-K., Self-Passivation of a LiNiO2 Cathode for a Lithium-Ion Battery through Zr Doping. *ACS Energy Letters* **2018,** *3* (7), 1634-1639.

23. Geng, C. X.; Liu, A. R.; Dahn, J. R., Impact of Aluminum Added to Ni-Based Positive Electrode Materials by Dry Particle Fusion. *Chemistry of Materials* **2020,** *32* (14), 6097-6104.

24. Wu, F.; Liu, N.; Chen, L.; Su, Y.; Tan, G.; Bao, L.; Zhang, Q.; Lu, Y.; Wang, J.; Chen, S.; Tan, J., Improving the reversibility of the H2-H3 phase transitions for layered Ni-rich oxide cathode towards retarded structural transition and enhanced cycle stability. *Nano Energy* **2019,** *59*, 50-57.

25. Mu, L. Q.; Kan, W. H.; Kuai, C. G.; Yang, Z. J.; Li, L. X.; Sun, C. J.; Sainio, S.; Avdeev, M.; Nordlund, D.; Lin, F., Structural and Electrochemical Impacts of Mg/Mn Dual Dopants on the LiNiO2 Cathode in Li-Metal Batteries. *Acs Applied Materials & Interfaces* **2020,** *12* (11), 12874-12882.

26. Seong, W. M.; Manthiram, A., Complementary Effects of Mg and Cu Incorporation in Stabilizing the Cobalt-Free LiNiO2 Cathode for Lithium-Ion Batteries. *Acs Applied Materials & Interfaces* **2020,** *12* (39), 43653-43664.

27. Yang, Z. J.; Mu, L. Q.; Hou, D.; Rahman, M. M.; Xu, Z. R.; Liu, J.; Nordlund, D.; Sun, C. J.; Xiao, X. H.; Lin, F., Probing Dopant Redistribution, Phase Propagation, and Local Chemical Changes in the Synthesis of Layered Oxide Battery Cathodes. *Advanced Energy Materials* **2021,** *11* (1).

28. Garcia, J. C.; Bareno, J.; Yan, J. H.; Chen, G. Y.; Hauser, A.; Croy, J. R.; Iddir, H., Surface Structure, Morphology, and Stability of Li(Ni1/3Mn1/3Co1/3)O-2 Cathode Material. *J Phys Chem C* **2017,** *121* (15), 8290-8299.

29. Sharifi-Asl, S.; Soto, F. A.; Nie, A. M.; Yuan, Y. F.; Asayesh-Ardakani, H.; Foroozan, T.; Yurkiv, V.; Song, B.; Mashayek, F.; Klie, R. F.; Amine, K.; Lu, J.; Balbuena, P. B.; Shahbazian-Yassar, R., Facet-Dependent Thermal Instability in LiCoO2. *Nano Letters* **2017,** *17* (4), 2165-2171.

30. Yan, P. F.; Zheng, J. M.; Gu, M.; Xiao, J.; Zhang, J. G.; Wang, C. M., Intragranular cracking as a critical barrier for high-voltage usage of layer-structured cathode for lithium-ion batteries. *Nat Commun* **2017,** *8*.

31. Zhang, H. L.; Omenya, F.; Yan, P. F.; Luo, L. L.; Whittingham, M. S.; Wang, C. M.; Zhou, G. W., Rock-Salt Growth-Induced (003) Cracking in a Layered Positive Electrode for Li-Ion Batteries. *Acs Energy Letters* **2017,** *2* (11), 2607-2615.

32. Zhu, J.; Chen, G. Y., Single-crystal based studies for correlating the properties and high-voltage performance of Li[NixMnyCo1-x-y]O-2 cathodes. *Journal of Materials Chemistry A* **2019,** *7* (10), 5463-5474.

33. Kim, M.; Zhu, J.; Li, L. Z.; Wang, C. M.; Chen, G. Y., Understanding Reactivities of Ni-Rich Li[NixMnyCo1-x-y]O-2 Single-Crystal Cathode Materials. *Acs Appl Energ Mater* **2020,** *3* (12), 12238-12245.

34. Kramer, D.; Ceder, G., Tailoring the Morphology of LiCoO2: A First Principles Study. *Chem Mater* **2009,** *21* (16), 3799-3809.

35. Liang, C.; Longo, R. C.; Kong, F.; Zhang, C.; Nie, Y.; Zheng, Y.; Cho, K., Ab initio Study on Surface Segregation and Anisotropy of Ni-rich LiNi1-2yCoyMnyO2 (NCM) ($y \leq 0.1$) Cathodes. *ACS Appl. Mater. Interfaces* **2018,** *10* (7), 6673-6680.

36. Bae, C.; Dupre, N.; Kang, B., Further Improving Coulombic Efficiency and Discharge Capacity in LiNiO2 Material by Activating Sluggish approximately 3.5 V Discharge Reaction. *ACS Appl Mater Interfaces* **2021,** *13* (20), 23760-23770.

37. Li, H. Y.; Zhang, N.; Li, J.; Dahn, J. R., Updating the Structure and Electrochemistry of LixNiO2 for 0 <= x <= 1. *Journal of the Electrochemical Society* **2018,** *165* (13), A2985-A2993.

38. Mesnier, A.; Manthiram, A., Synthesis of LiNiO2 at Moderate Oxygen Pressure and Long-Term Cyclability in Lithium-Ion Full Cells. *ACS Applied Materials & Interfaces* **2020,** *12* (47), 52826-52835.

39. Heo, K.; Lee, J.; Song, Y.-W.; Kim, M.-Y.; Jeong, H.; DoCheon, A.; Jaekook, K.; Lim, J., Synthesis and Electrochemical Performance Analysis of LiNiO2 Cathode Material Using Taylor-Couette Flow-Type Co-Precipitation Method. *Journal of The Electrochemical Society* **2021,** *168* (1), 010521.

40. Ma, Z. P.; Shao, G. J.; Fan, Y. Q.; Wang, G. L.; Song, J. J.; Liu, T. T., Tunable Morphology Synthesis of LiFePO4 Nanoparticles as Cathode Materials for Lithium Ion Batteries. *Acs Applied Materials & Interfaces* **2014,** *6* (12), 9236-9244.

41. Bai, P.; Cogswell, D. A.; Bazant, M. Z., Suppression of Phase Separation in LiFePO4 Nanoparticles During Battery Discharge. *Nano Letters* **2011,** *11* (11), 4890-4896.

42. Wang, Y.; Cao, G. Z., Developments in nanostructured cathode materials for high-performance lithium-ion batteries. *Advanced Materials* **2008,** *20* (12), 2251-2269.

43. Garcia, J. C.; Bareno, J.; Chen, G. Y.; Croy, J. R.; Iddir, H., Strain-driven surface reconstruction and cation segregation in layered Li(Ni1-x-yMnxCoy)O-2 (NMC) cathode materials. *Phys Chem Chem Phys* **2020,** *22* (42), 24490-24497.

44. Wang, C.; Zhang, R.; Kisslinger, K.; Xin, H. L., Atomic-Scale Observation of O1 Faulted Phase-Induced Deactivation of LiNiO2 at High Voltage. *Nano Lett* **2021,** *21* (8), 3657-3663.

45. Das, H.; Urban, A.; Huang, W.; Ceder, G., First-Principles Simulation of the (Li–Ni–Vacancy)O Phase Diagram and Its Relevance for the Surface Phases in Ni-Rich Li-Ion Cathode Materials. *Chem Mater* **2017,** *29* (18), 7840-7851.

46. Cho, E.; Seo, S. W.; Min, K., Theoretical Prediction of Surface Stability and Morphology of LiNiO2 Cathode for Li Ion Batteries. *Acs Applied Materials & Interfaces* **2017,** *9* (38), 33257-33266.

47. Mu, L. Q.; Yang, Z. Z.; Tao, L.; Waters, C. K.; Xu, Z. R.; Li, L. X.; Sainio, S.; Du, Y. G.; Xin, H. L.; Nordlund, D.; Lin, F., The sensitive surface chemistry of Co-free, Ni-rich layered oxides: identifying experimental conditions that influence characterization results. *Journal of Materials Chemistry A* **2020,** *8* (34), 17487-17497.

48. Deng, T.; Fang, X. L.; Cao, L. S.; Chen, J.; Hou, S. Y.; Ji, X.; Chen, L.; Li, S.; Zhou, X. Q.; Hu, E. Y.; Su, D.; Yang, X. Q.; Wang, C. S., Designing In-Situ-Formed Interphases Enables Highly Reversible Cobalt-Free LiNiO2 Cathode for Li-ion and Li-metal Batteries. *Joule* **2019,** *3* (10), 2550-2564.

49. Flamme, B.; Swiatowska, J.; Haddad, M.; Phansavath, P.; Ratovelomanana-Vidal, V.; Chagnes, A., Sulfone Based-Electrolytes for Lithium-Ion Batteries: Cycling Performances and Passivation Layer Quality of Graphite and LiNi1/3Mn1/3Co1/3O2 Electrodes. *Journal of the Electrochemical Society* **2020,** *167* (7).

50. Hong, L.; Hu, L.; Freeland, J. W.; Cabana, J.; Öğüt, S.; Klie, R. F., Electronic Structure of LiCoO2 Surfaces and Effect of Al Substitution. *The Journal of Physical Chemistry C* **2019,** *123* (14), 8851-8858.

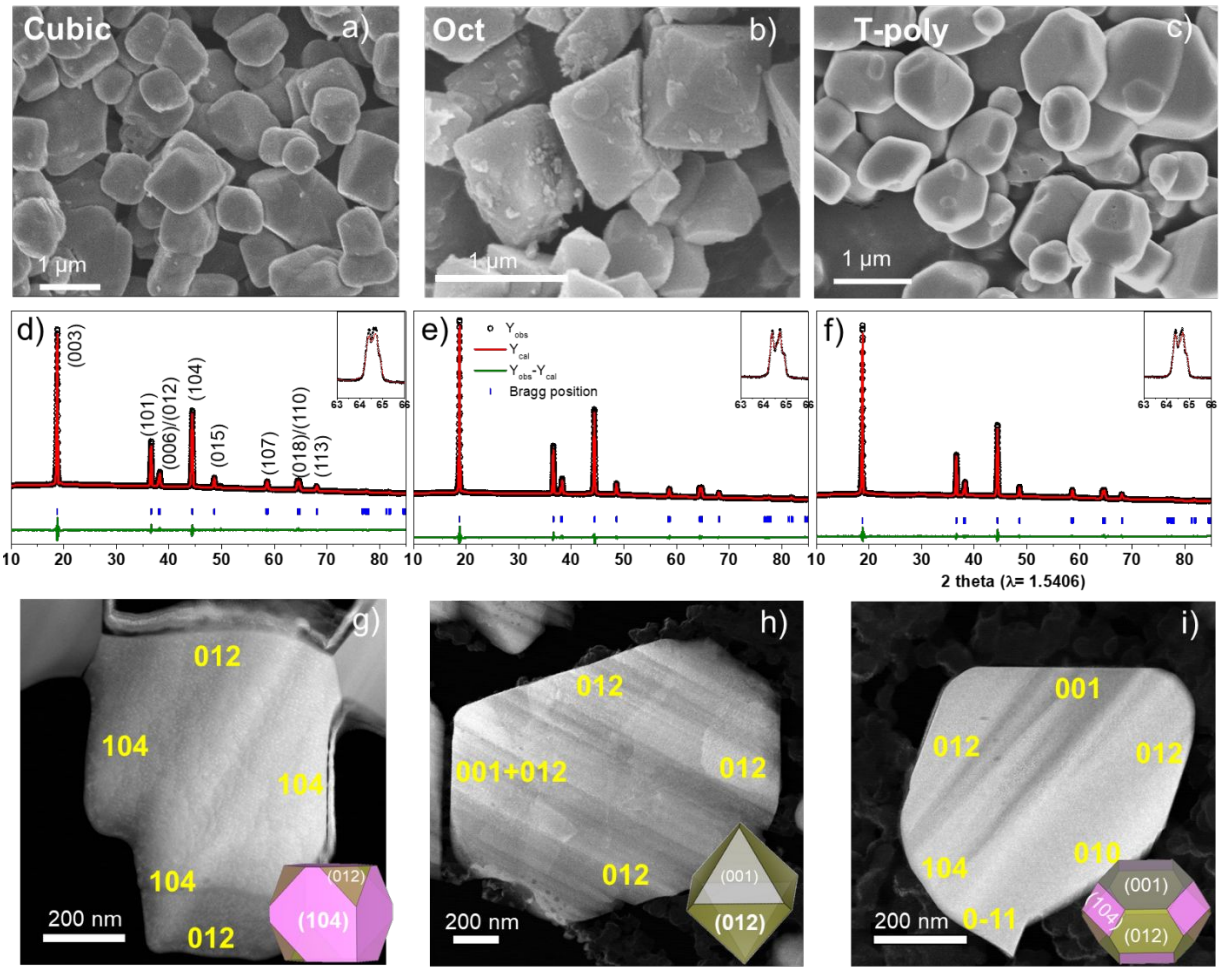

Figure 1. SEM images (a-c), XRD patterns (d-f) and HRTEM images (g-i) of the as-synthesized single-crystal $LiNiO_2$ samples: a, d, g) Cubic-SC-LNO, b, e, h) Oct-SC-LNO and c, f, i) T-poly-SC-LNO. Insets in d-f) show the peak splitting of (018)/(110) doublets. Insets in g-i) show particle shapes with surface facets as indexed.

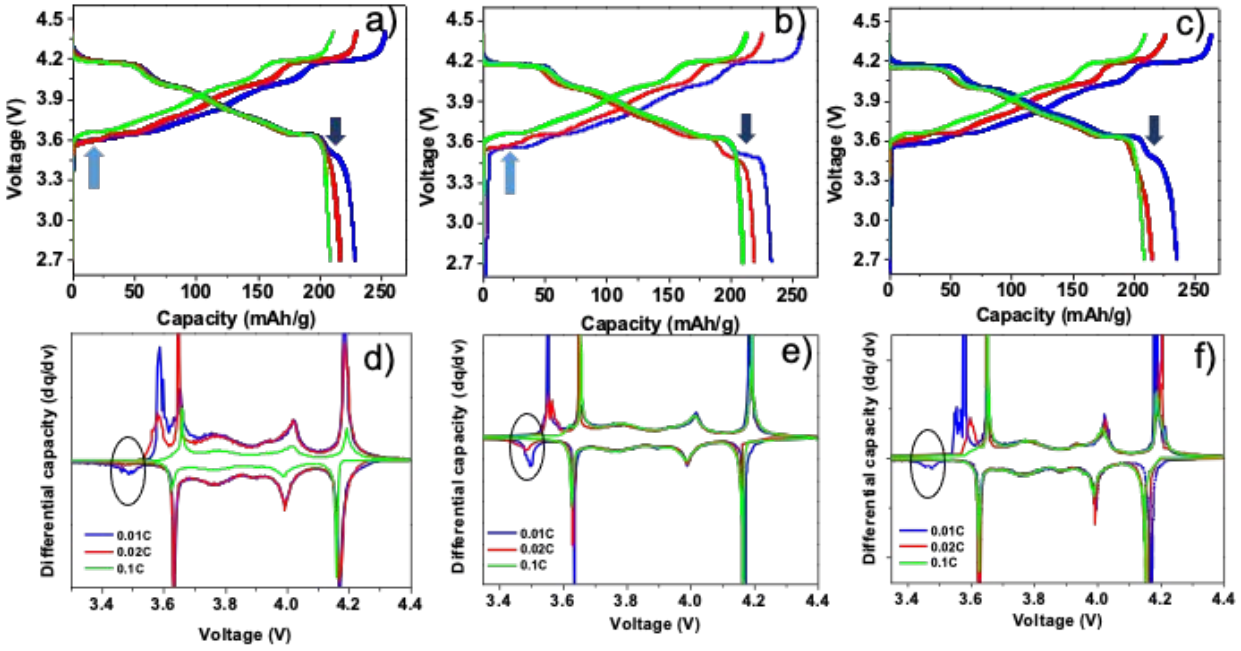

Figure 2. Voltage profiles (a-c) and the corresponding *d*Q/*d*V plots (d-f) of the single-crystal $LiNiO_2$ cathodes cycled at 0.01C, 0.02C and 0.1C rates: a, d) Cubic-SC-LNO, b, e) Oct-SC-LNO and c, f) T-poly-SC-LNO.

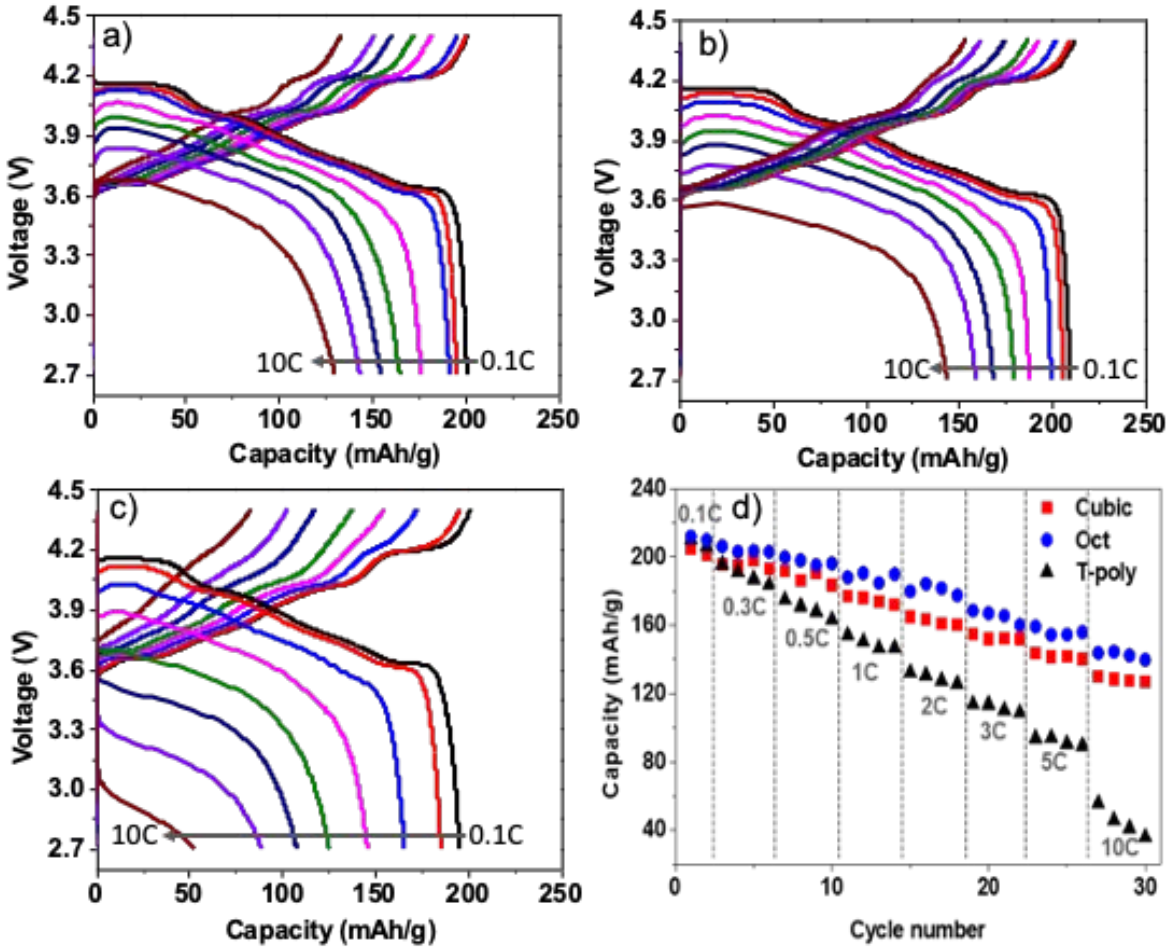

Figure 3. Voltage profiles of the SC-LNO cathodes cycled at various C-rates: a) Cubic-SC-LNO, b) Oct-SC-LNO and c) T-poly-SC-LNO. d) Rate capability comparison of the cathodes. The cells were charged at the same 0.1C rate while the discharge rate varied from 0.1C to 10C. Coulombic efficiencies are provided in Supporting Information (Fig. S1).

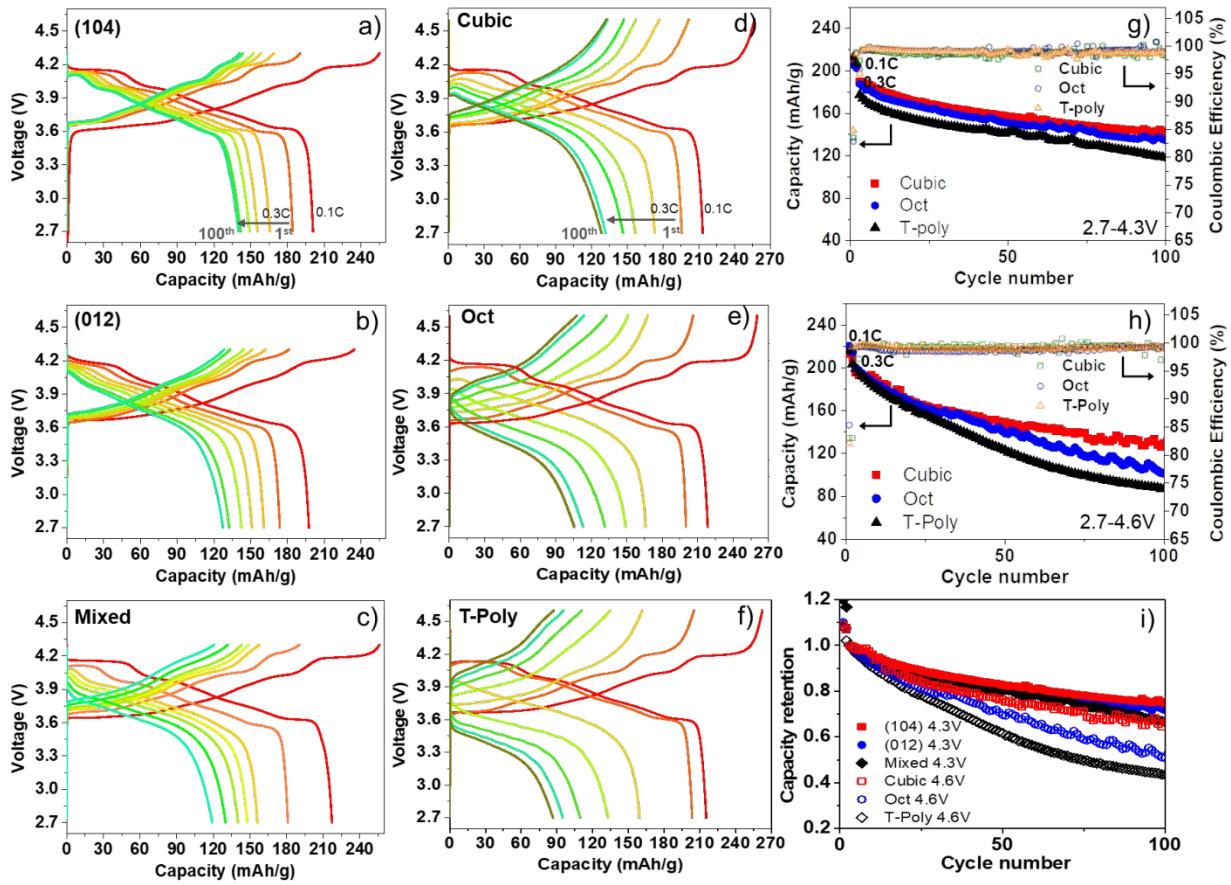

Figure 4. Voltage profiles of the SC-LNO cathodes collected during the first 100 cycles between 2.7-4.3 V (a-c) and 2.7-4.6 V (d-f). Half-cells were cycled at 0.1C for the first two cycles and then at 0.3C for the rest. Data shown are plotted in every 20 cycles after the first cycle. a, d) Cubic-SC-LNO, b, e) Oct-SC-LNO and c, f) T-poly-SC-LNO. g) discharge capacity and coulombic efficiency as a function of cycle number in 2.7-4.3 V, h) discharge capacity and coulombic efficiency as a function of cycle number in 2.7-4.6 V, and i) capacity retention as a function of cycle number.

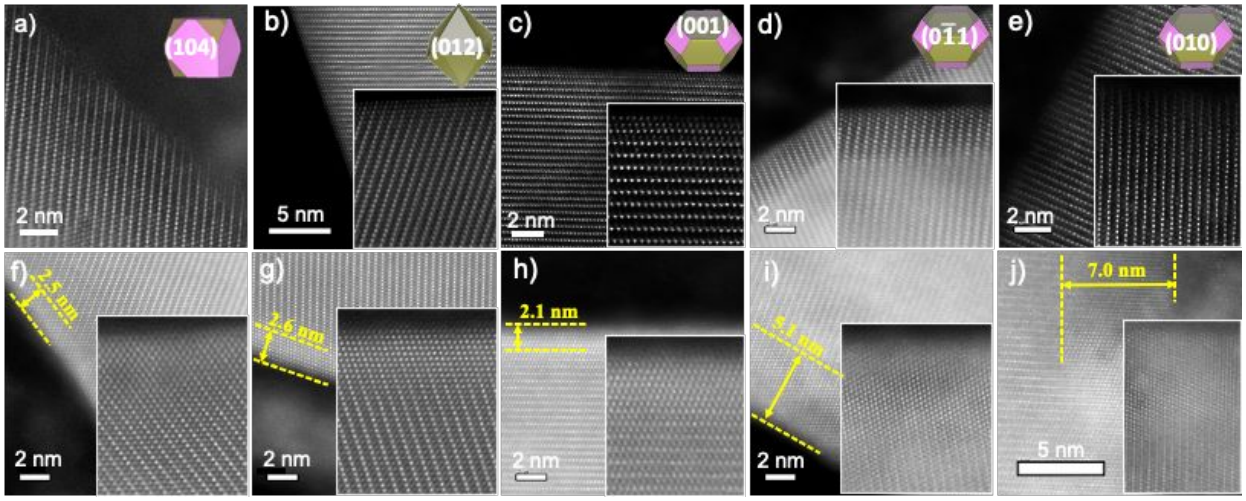

Figure 5. STEM-HADDF images collected on various facets of the pristine (a-e) and cycled (f-j) SC-LNO samples: (a, f) (104) of Cubic-SC-LNO, (b, g) (012) of Oct-SC-LNO, (c, h) (001) of T-poly-SC-LNO, (d, i) (0$\bar{1}$1) of T-poly-SC-LNO, and (e, j) (010) of T-poly-SC-LNO. Cycled samples were recovered at discharged state after 100 cycles between 2.7 and 4.6 V.

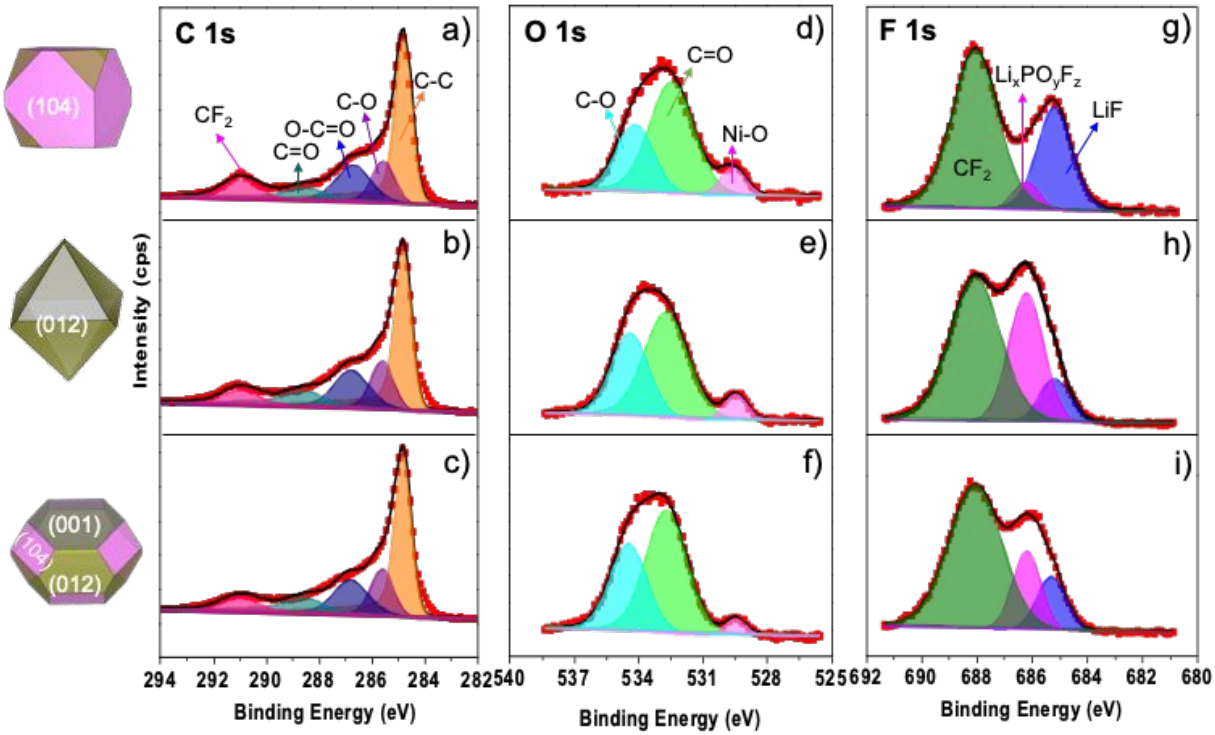

Figure 6. XPS analysis data collected on the recovered SC-LNO cathodes after 100 cycles between 2.7 and 4.6 V at 0.3C: (a-c) C 1*s*, (d-f) O 1*s*, and (g-i) F 1*s*. (a, d, g) are from Cubic-SC-LNO, (b, e, h) are from Oct-SC-LNO, and (c, f, i) are from T-poly-SC-LNO.

Table 1. Rietveld refinement results of the SC-LNO XRD patterns

Sample	***a*=*b* (Å)**	***c* (Å)**	**γ(°)**	***V* (Å^3)**	**Li/Ni mixing**
Cubic-SC-LNO	2.8793(6)	14.2035(4)	120	101.977(4)	5.7%
Oct-SC-LNO	2.8792(5)	14.2081(3)	120	102.002(3)	6.6%
T-poly-SC-LNO	2.8788(3)	14.2028(3)	120	101.932(3)	4.9%